

A higher-than-predicted measurement of iron opacity at solar interior temperatures

J. E. Bailey¹, T. Nagayama¹, G. P. Loisel¹, G. A. Rochau¹, C. Blancard², J. Colgan³, Ph. Cosse², G. Faussurier², C. J. Fontes³, F. Gilleron², I. Golovkin⁴, S. B. Hansen¹, C. A. Iglesias⁵, D. P. Kilcrease³, J. J. MacFarlane⁴, R. C. Mancini⁶, S. N. Nahar⁷, C. Orban⁷, J.-C. Pain², A. K. Pradhan⁷, M. Sherrill³ & B. G. Wilson⁵

Nearly a century ago it was recognized¹ that radiation absorption by stellar matter controls the internal temperature profiles within stars. Laboratory opacity measurements, however, have never been performed at stellar interior conditions, introducing uncertainties in stellar models^{2–5}. A particular problem arose^{2,3,6–8} when refined photosphere spectral analysis^{9,10} led to reductions of 30–50 per cent in the inferred amounts of carbon, nitrogen and oxygen in the Sun. Standard solar models¹¹ using the revised element abundances disagree with helioseismic observations that determine the internal solar structure using acoustic oscillations. This could be resolved if the true mean opacity for the solar interior matter were roughly 15 per cent higher than predicted^{2,3,6–8}, because increased opacity compensates for the decreased element abundances. Iron accounts for a quarter of the total opacity^{2,12} at the solar radiation/convection zone boundary. Here we report measurements of wavelength-resolved iron opacity at electron temperatures of 1.9–2.3 million kelvin and electron densities of $(0.7–4.0) \times 10^{22}$ per cubic centimetre, conditions very similar to those in the solar region that affects the discrepancy the most: the radiation/convection zone boundary. The measured wavelength-dependent opacity is 30–400 per cent higher than predicted. This represents roughly half the change in the mean opacity needed to resolve the solar discrepancy, even though iron is only one of many elements that contribute to opacity.

In the region of the solar radiation/convection zone boundary¹¹, the electron temperature $T_e \approx 2.1 \times 10^6$ K, the electron density $n_e \approx 9 \times 10^{22}$ cm⁻³, and the iron opacity arises mainly from L-shell bound-bound and bound-free transitions in the 6–16 Å spectral range. There are multiple processes involved in modelling these transitions, including the electron energy-level structure, photoionization, and continuum lowering. A theoretical challenge is an accurate description of excited atomic states, which are prevalent at solar interior temperatures. Plasma line-broadening models are both untested and important in this regime, because photons are more readily transported in the ‘windows’ between the lines and broader lines tend to close the opacity windows. Finally, there is at present no consensus on how to model the autoionizing levels adequately¹³.

Stellar interior energy transport calculations require the Rosseland mean¹⁴, a harmonic average over photon energy. The large range of stellar constituents and conditions makes it impractical to measure all the mean opacities that are needed. Therefore, here we measured wavelength-dependent opacities over a range of densities and temperatures in an attempt to understand the different physical processes.

There were three main impediments^{15,16} to laboratory opacity measurements at stellar interior conditions that were surmounted by the Sandia Z facility^{16–18}: (1) a macroscopic sample had to be uniformly heated to stellar interior conditions; (2) the sample had to contain an electron population distribution that could be described by the local thermodynamic

equilibrium (LTE) (in the Sun, this distribution is enforced by the radiation field); and (3) a spectrally smooth X-ray backlight was needed that was sufficiently bright to overcome sample self-emission. A spectrometer that views the backlight directly and through the sample determines the spectrally resolved transmission. The opacity is inferred by taking the natural log of the transmission and dividing by the areal density. The first such measurements for high-energy-density matter¹⁹ were published in 1988, at temperatures about a factor of four lower than at the solar radiation/convection zone boundary. Later experiments^{15,20} refined the method, but the maximum temperature did not exceed approximately 0.9×10^6 K.

An important step forward was realized in 2007 when the Z-facility opacity science platform^{16,17} provided iron transmission laboratory measurements at 1.8×10^6 K. These experiments created the iron charge states that exist in the solar radiation/convection zone boundary region, but T_e and n_e were still too low to test solar opacity models definitively. Higher- T_e and n_e measurements have now been developed by exploiting the increased X-ray power at the Z facility¹⁸ and sample design improvements²¹. The Fe/Mg sample foils are heated during the ~ 10 ns radiation source assembly phase (Fig. 1 and Methods) and backlit when the radiation source stagnation provides a backlight of duration ~ 3 ns and spectral radiance equivalent to a ~ 350 eV Planckian. The Planck-equivalent radiation flux of ~ 210 eV at the sample drives the electronic populations to form a replica of the LTE distribution. The conditions are controlled by tamping the sample expansion with different thicknesses of plastic (CH) and Be. The backlight time is fixed relative to the heating radiation, so heavily tamped samples that expand more slowly are at a higher density and temperature at the time the absorption spectrum is measured (Extended Data Fig. 1).

We performed measurements over a range of T_e/n_e values to gain an understanding of the physical processes that control the opacity (see Methods). The T_e/n_e values inferred using K-shell spectroscopic analysis²² of Mg intermixed with the Fe were 1.91×10^6 K/ 7×10^{21} cm⁻³; 1.97×10^6 K/ 2×10^{22} cm⁻³; 2.11×10^6 K/ 3.1×10^{22} cm⁻³; and 2.26×10^6 K/ 4×10^{22} cm⁻³. The T_e and n_e accuracies are $\pm 4\%$ and $\pm 25\%$, respectively. The highest T_e reported here exceeds the radiation/convection zone boundary temperature by approximately 4%, whereas n_e is a factor of ~ 2.3 lower.

The measurements at these four conditions (Fig. 2) show that as the T_e/n_e values are increased, the opacity rises, the prominent line features shrink with respect to the nearby quasi-continuum, the ‘windows’ between the lines fill in, and the lines become broader. The SCRAM²³ opacity model (Fig. 2) predicts similar trends, but the degree of change effected by raising T_e and n_e is strikingly smaller. The agreement is best at the lowest T_e/n_e conditions and deteriorates as T_e and n_e increase.

A comparison of the 2.11×10^6 K/ 3.1×10^{22} cm⁻³ measured opacity spectrum with several opacity models is shown in Fig. 3. The OPAL²⁴

¹Sandia National Laboratories, 1515 Eubank SE, Albuquerque, New Mexico 87185-1196, USA. ²Commissariat à l’Énergie Atomique (CEA) et aux Énergies Alternatives, F-91297 Arpajon, France. ³Los Alamos National Laboratory, Bikini Atoll Road, Los Alamos, New Mexico 87545, USA. ⁴Prism Computational Sciences, 455 Science Drive, Suite 140, Madison, Wisconsin 53711, USA. ⁵Lawrence Livermore National Laboratory, 7000 East Avenue, Livermore, California 94550-9234, USA. ⁶University of Nevada, 1664 North Virginia Street, Reno, Nevada 89557, USA. ⁷Ohio State University, 140 West 18th Avenue, Columbus, Ohio 43210, USA.

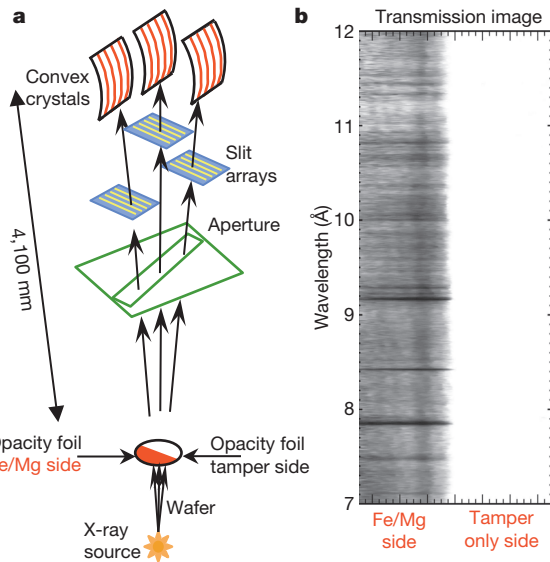


Figure 1 | Experiment diagram and example transmission image. **a**, Three to four spectrometers view the ‘half-moon’-shaped tamped iron/magnesium sample (not to scale). Each uses multiple slits to project spatially resolved images onto a convex crystal that disperses the spectrum before recording on film (not shown). The set-up measures the unattenuated (tamper only) and the attenuated (tamper plus FeMg) spectra in the same experiment. **b**, A spatially resolved and spectrally resolved transmission image is obtained by dividing the attenuated spectral image by the unattenuated image. Darker regions correspond to higher absorption. The white portion of the image corresponds to $\sim 100\%$ transmission.

and OP^{25,26} models are most frequently used in astrophysics, although the OPAS model has recently been used¹² to calculate solar opacities. Unfortunately, wavelength-dependent OPAL calculations are no longer available. OP calculations generally yield values lower than the data values and the wavelengths of the strong spectral features disagree (Fig. 3a). The latter implies that the OP energy-level structure is not sufficiently accurate and the former is consistent with a hypothesis that OP does not account for all of the transitions present in the actual solar plasma. Comparisons with the ATOMIC²⁷, OPAS¹², and SCO-RCG²⁸ models (Fig. 3b) show that these models also yield values notably lower than the data values over most of the spectral range. The strong bound-bound feature wavelengths agree reasonably well, but none of these models reproduces the measured opacity spectra. These models have been more recently formulated or updated than the OP model and they exploit the advances in computing power that have occurred in the last decade. OP and ATOMIC use line-by-line atomic physics calculations while the other models employ a hybrid approach that combines line-by-line calculations for the strongest transitions and a statistical treatment for the myriad weaker transitions.

The predicted Rosseland mean opacities for iron are lower than the measured Rosseland mean values by 1.75, 1.67, 1.53, 1.75, and 1.57 for the OP, SCRAM, OPAS, ATOMIC, and SCO-RCG models, respectively. These comparisons use the Be-tamped measurement conditions ($2.11 \times 10^6 \text{ K}/3.1 \times 10^{22} \text{ cm}^{-3}$), account for the instrument resolution effect, and are restricted to the 7.0–12.7 Å range reported here. The Be-tamper data reflect the measurements at high T_e/n_e with the best accuracy and they generally support the validity of the thick-CH measurements (see Methods). These differences are large compared to the roughly $\pm 11\%$ experimental uncertainty in the Rosseland mean. Ratios of the experimental and model opacities as a function of wavelength further quantify the discrepancies (Fig. 3c). The differences between the ratios calculated for the various models at specific wavelengths can help formulate hypotheses for the discrepancies.

First, the predicted opacity is lower than the measurement by a factor of 1.3–1.9 in the short-wavelength (7–10 Å) range. Models predict that

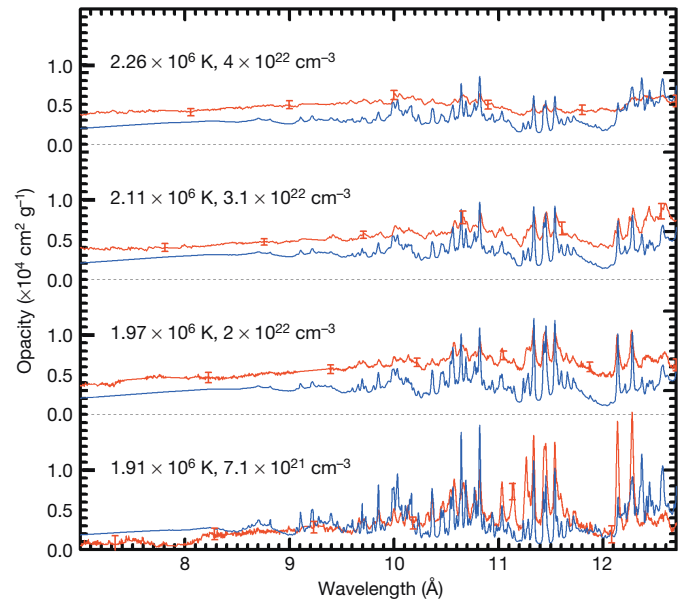


Figure 2 | Measured iron opacity spectra at four T_e/n_e values compared with calculations. The SCRAM²³ model calculations (blue lines) account for the instrument resolution. Red lines denote the measurements and the error bars represent 1σ uncertainties. The measurements combine information from 22 separate experiments, each with three or four independent spectrometers that each record 4–6 spectra. The numbers of experiments used to infer the average opacities presented here were as follows: six for the $1.91 \times 10^6 \text{ K}/7 \times 10^{21} \text{ cm}^{-3}$ results; one for the $1.97 \times 10^6 \text{ K}/2 \times 10^{22} \text{ cm}^{-3}$ results; five for the $2.11 \times 10^6 \text{ K}/3.1 \times 10^{22} \text{ cm}^{-3}$ results; and ten for the $2.26 \times 10^6 \text{ K}/4 \times 10^{22} \text{ cm}^{-3}$ results.

bound–free transitions dominate over bound–bound transitions for wavelengths shorter than $\sim 9.5 \text{ Å}$ (Extended Data Fig. 3). If the data are correct (see below and Methods), then two possible explanations are that (1) models neglect additional bound–bound features in the short wavelength range or (2) predictions for the photoionization bound–free contribution are low in this spectral range. Second, the measured opacities in the windows between the strong spectral features are higher than the model predictions. At the same time, the peak opacity agreement of the strong spectral features varies from feature to feature and from model to model. We note that even among the model predictions there are $\sim 50\%$ variations in the strength of certain strong spectral features. Furthermore, the measured widths of the strong prominent line features are broader than the predictions. These facts together suggest that there are missing transitions from the models, the Stark and/or autoionization broadening of the line features is larger than predicted, or both.

The comparisons imply that revisions are needed to the current descriptions of photon absorption by atoms in high-energy-density plasmas. This finding has broad implications for astrophysics and in the laboratory, so it is essential to determine whether the problem lies with the experimental methods. We established experimental reliability and reproducibility by incorporating approximately 450 spectra recorded in 22 separate experiments. We examined many possible systematic errors, including transmission errors, plasma diagnostic accuracy, departures from LTE, extraneous background, sample flaws, spatial and temporal gradients, and tamper attenuation and emission. These effects were found to be too small to influence the conclusions drawn above.

The measured iron opacity affects our understanding of the solar interior. We evaluate the impact by first computing the wavelength-dependent opacity for the solar interior composition⁹ and the OP opacities^{25,26} at $T_e = 2.11 \times 10^6 \text{ K}$ and $n_e = 3.1 \times 10^{22} \text{ cm}^{-3}$ (Fig. 4), the values of the Be-tamped experiment. We then replace the OP iron contribution in the measured wavelength range with the experimental results, while the opacity contributions from the other solar matter constituents are kept the same. The impact on the solar mixture Rosseland mean depends

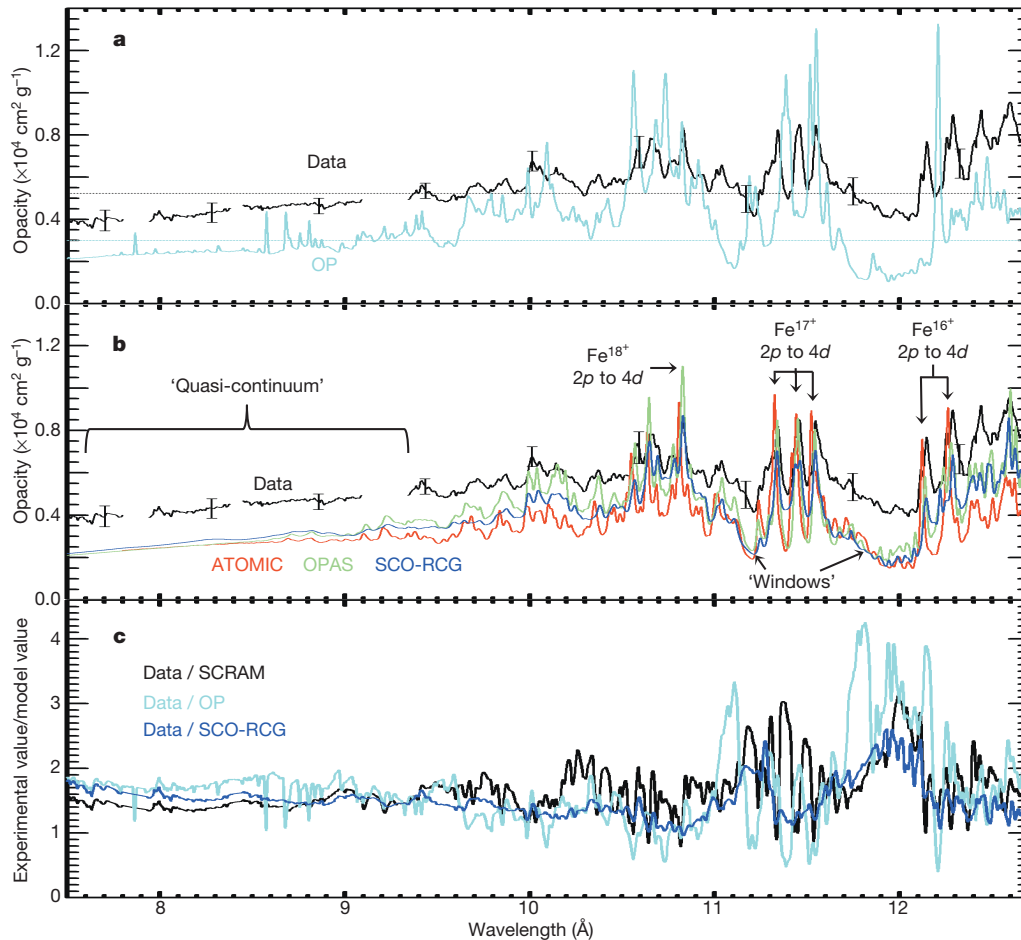


Figure 3 | Comparisons of iron opacity spectra with multiple models at the solar radiation/convection zone boundary temperature. The $T_e = 2.11 \times 10^6$ K, $n_e = 3.1 \times 10^{22}$ cm $^{-3}$ conditions displayed here were deemed to be the most accurate; the opacity represents an average obtained by combining information from five separate experiments with four independent spectrometers. The calculations account for the instrument resolution and

the experiment error bars represent 1σ uncertainties. **a**, Comparison with the OP model^{25,26} that is used for solar modelling. The dashed lines are the Rosseland mean opacities calculated for this wavelength range. **b**, Comparisons with the ATOMIC, OPAS and SCO-RCG models. **c**, Ratio of the experiment opacity to the opacities modelled by SCRAM, OP and SCO-RCG.

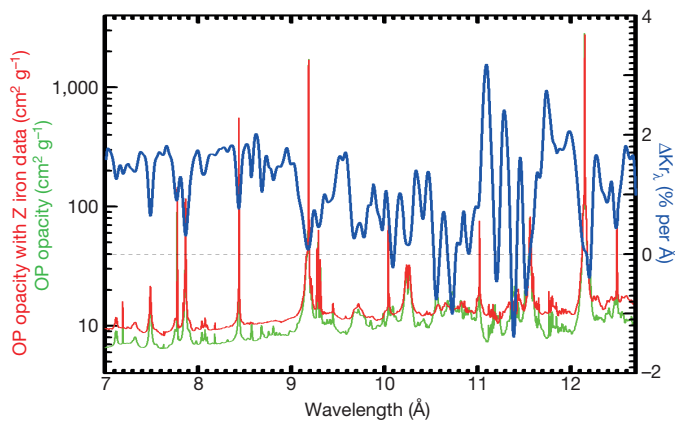


Figure 4 | Measured iron opacity impact on solar mixture Rosseland mean. The opacity of a plasma with solar composition⁹ is calculated with OP^{25,26} (green line; log scale on left axis) at the experiment conditions ($T_e = 2.11 \times 10^6$ K, $n_e = 3.1 \times 10^{22}$ cm $^{-3}$). The opacity for the same plasma using the measured iron opacity is generally higher (red line; log scale on left axis). The Rosseland mean opacity percentage change per unit wavelength (ΔK_r) is denoted with a blue line (linear scale on right axis). Spectral features where the blue curve is below the dashed line reduce the solar mixture Rosseland mean and features above the dashed line raise it.

on the ratio of the measured to calculated iron opacity (Fig. 3c), the Rosseland mean weighting function, and the relative importance of the iron contribution to the total opacity at each wavelength. The percentage change per unit wavelength in the Rosseland mean caused by using the experimental iron measurement as a function of wavelength (Fig. 4) helps to identify which spectral features have the most impact on the Sun's opacity. Integrated over wavelength, the Rosseland mean for this mixture of solar constituents is $7 \pm 3\%$ higher when the experimental iron opacity is used. This is about half of the opacity adjustment required⁸ to restore agreement between standard solar models¹¹ and helioseismology.

The present experiments imply that model corrections are probably needed for all the solar constituents ionized into the L-shell, including Ni, Cr, Ti, and Ca. Experiments with Ni and Cr are in progress, both to help evaluate hypotheses for the model–experiment discrepancy observed for iron and to determine whether additional revisions to the solar opacity are appropriate. Future work will attempt to increase the experimental electron density by a factor of 2.3, to achieve opacity measurements at the T_e and n_e that are believed to exist at the solar radiation/convection zone boundary region.

Online Content Methods, along with any additional Extended Data display items and Source Data, are available in the online version of the paper; references unique to these sections appear only in the online paper.

Received 17 September; accepted 3 November 2014.

1. Eddington, A. S. *The Internal Constitution of the Stars* (Cambridge Univ. Press, 1926).

2. Basu, S. & Antia, H. M. Helioseismology and solar abundances. *Phys. Rep.* **457**, 217–283 (2008).
3. Basu, S., Grevesse, N., Mathis, S. & Turck-Chièze, S. Understanding the internal chemical composition and physical processes of the solar interior. *Space Sci. Rev.* <http://dx.doi.org/10.1007/s11214-014-0035-9> (2014).
4. Christensen-Dalsgaard, J. in *Proc. IAU Symp. No. 258, The Ages of Stars (2008)* (eds Mamajek, E. E., Soderblom, D. R. & Wyse, R. F. G.) 431–442 (International Astronomical Union, 2009).
5. Delahaye, F. & Pinsonneault, M. Comparison of radiative accelerations obtained with atomic data from OP and OPAL. *Astrophys. J.* **625**, 563–574 (2005).
6. Bahcall, J. N., Serenelli, A. M. & Pinsonneault, M. How accurately can we calculate the depth of the solar convective zone? *Astrophys. J.* **614**, 464–471 (2004).
7. Turck-Chièze, S. *et al.* Surprising Sun: a new step towards a complete picture? *Phys. Rev. Lett.* **93**, 211102 (2004).
8. Serenelli, A. M., Basu, S., Ferguson, J. W. & Asplund, M. New solar composition: the problem with solar models revisited. *Astrophys. J.* **705**, L123–L127 (2009).
9. Asplund, M., Grevesse, N., Sauval, J. A. & Scott, P. The chemical composition of the Sun. *Annu. Rev. Astron. Astrophys.* **47**, 481–522 (2009).
10. Caffau, E. *et al.* Solar chemical abundances determined with a CO5BOLD 3D model atmosphere. *Sol. Phys.* **268**, 255–269 (2011).
11. Bahcall, J. N. *et al.* Standard solar models and the uncertainties in predicted capture rates of solar neutrinos. *Rev. Mod. Phys.* **54**, 767–799 (1982).
12. Blancard, C., Cosse, Ph. & Faussurier, G. Solar mixture opacity calculations using detailed configuration and level accounting treatments. *Astrophys. J.* **745**, 10 (2012).
13. Nahar, S. N., Pradhan, A. K., Chen, G.-X. & Eissner, W. Highly excited core resonances in photoionization of Fe XVII: implications for plasma opacities. *Phys. Rev. A* **83**, 053417 (2011).
14. Rosseland, S. Note on the absorption of radiation within a star. *Mon. Not. R. Astron. Soc.* **84**, 525–528 (1924).
15. Perry, T. S. *et al.* Absorption experiments on x-ray-heated mid-Z constrained samples. *Phys. Rev. E* **54**, 5617–5631 (1996).
16. Bailey, J. E. *et al.* Experimental investigation of opacity models for stellar interior, inertial fusion, and high energy density plasmas. *Phys. Plasmas* **16**, 058101 (2009).
17. Bailey, J. E. *et al.* Iron-plasma transmission measurements at temperatures above 150 eV. *Phys. Rev. Lett.* **99**, 265002 (2007).
18. Rochau, G. A. *et al.* ZAPP: the Z Astrophysical Plasma Properties collaboration. *Phys. Plasmas* **21**, 056308 (2014).
19. Davidson, S. J. *et al.* Investigation of the opacity of hot, dense aluminum in the region of its K edge. *Appl. Phys. Lett.* **52**, 847–849 (1988).
20. Foster, J. M. *et al.* L-shell absorption spectrum of an open-M-shell germanium plasma: comparison of experimental data with a detailed configuration-accounting calculation. *Phys. Rev. Lett.* **67**, 3255–3258 (1991).
21. Nash, T. J., Rochau, G. A. & Bailey, J. E. Design of dynamic Hohlräum opacity samples to increase measured sample density on Z. *Rev. Sci. Instrum.* **81**, 10E518 (2010).
22. Nagayama, T. *et al.* Control and diagnosis of temperature, density, and uniformity in x-ray heated iron/magnesium samples for opacity measurements. *Phys. Plasmas* **21**, 056502 (2014).
23. Hansen, S., Bauche, J., Bauche-Arnoult, C. & Gu, M. Hybrid atomic models for spectroscopic plasma diagnostics. *High Energy Density Phys.* **3**, 109–114 (2007).
24. Iglesias, C. A. & Rogers, F. J. Opacities for the solar radiative interior. *Astrophys. J.* **371**, 408–417 (1991).
25. Seaton, M. J., Yu, Y., Mihalas, D. & Pradhan, A. K. Opacities for stellar envelopes. *Mon. Not. R. Astron. Soc.* **266**, 805–828 (1994).
26. Badnell, N. R. *et al.* Updated opacities from the opacity project. *Mon. Not. R. Astron. Soc.* **360**, 458–464 (2005).
27. Colgan, J. *et al.* Light element opacities from ATOMIC. *High Energy Density Phys.* **9**, 369–374 (2013).
28. Porcherot, Q., Pain, J.-C., Gilleron, F. & Blenski, T. A consistent approach for mixed detailed and statistical calculation of opacities in hot plasmas. *High Energy Density Phys.* **7**, 234–239 (2011).

Acknowledgements Sandia is a multiprogramme laboratory operated by Sandia Corporation, a Lockheed Martin Company, for the United States Department of Energy under contract DE-AC04-94AL85000. The Los Alamos National Laboratory is operated by Los Alamos National Security, LLC, for the NNSA of the US DOE under contract number DE-AC5206NA25396. J.E.B. acknowledges support from a DOE High Energy Density Laboratory Plasmas grant. A.K.P. and C.O. also acknowledge support from a DOE High Energy Density Laboratory Plasmas grant. We appreciate the efforts of the entire Z facility team. We thank S. Turck-Chièze, H. Morris, and M. Pinsonneault for discussions. We also thank R. W. Lee for critiquing the manuscript. We appreciate support for the experiments provided by R. J. Leeper, J. L. Porter, M. K. Matzen and M. Herrmann.

Author Contributions These measurements were conceived and planned by J.E.B. and G.A.R. J.E.B. was the primary author of the manuscript, with important contributions from T.N. Experiments were conducted by J.E.B., G.A.R. and G.P.L. The Z-facility data were analysed by T.N., J.E.B. and G.P.L., with assistance from G.A.R., C.A.I., B.G.W., I.G., J.J. M. and R.C.M. OPAS calculations were performed by C.B., G.F. and Ph.C. ATOMIC calculations were performed by J.C., with assistance from C.F., D.P.K. and M.S. SCRAM calculations were provided by S.B.H. SCO calculations were performed by J.-C.P. and F.G. OP calculations were performed by C.O., with assistance from A.K.P. and S.N.N. All authors discussed the results, commented on the manuscript, and contributed to the interpretation.

Author Information Reprints and permissions information is available at www.nature.com/reprints. The authors declare no competing financial interests. Readers are welcome to comment on the online version of the paper. Correspondence and requests for materials should be addressed to J.E.B. (jebaile@sandia.gov).

METHODS

Experimental methods. The Z-facility opacity science platform^{16–18,22,29,30} samples consist of thin ‘half-moon’-shaped FeMg films sandwiched by low-Z tamper materials (Extended Data Fig. 1, Extended Data Table 1). Optical microscopy confirmed that the samples were free of non-uniformities that can artificially reduce the inferred opacity. Profilometry verified that the ‘half-moon’ boundary sharpness was approximately 10 μm or less. Profilometry and interferometry sample thickness measurements provided an upper bound on the sample areal density, because the fabrication methods produce thin films with densities lower than the bulk density. Rutherford backscattering spectrometry (RBS)³¹ provided primary areal density measurements with an accuracy of better than $\sim 4\%$ for the individual sample constituents. Three separate RBS laboratories measured many of the sample areal densities with an average standard deviation of $\pm 3\%$. A small group of samples was also measured by weighing a precisely determined sample area. This measurement agreed with the RBS measurements.

The results described here are based on 22 Z experiments conducted over a three-year period. The diagnostic configuration was refined over the course of this work and the transmission determination method depends on the configuration. Four X-ray crystal spectrometers were employed, configured to view the backlight at a combination of angles with respect to the Z-pinch axis: $+9^\circ$, -9° and 0° . These spectrometers provide multiple simultaneous measurements of the attenuated and unattenuated backlight spectra from each single experiment. Here, the term ‘attenuated’ refers to the reduction in backlight intensity by the FeMg layer; all signals include the attenuation by the low-Z tamper plasma.

The spectrometer fields of view were restricted by a aperture 1 mm wide located 17 mm above the sample. An array of either four or six 50- μm -wide slits provided a spatial resolution of $\sim 100 \mu\text{m}$ perpendicular to the ‘half-moon’ boundary. Each slit projects a nominally identical spatially resolved and spectrally resolved image onto the detector. The collection of slit-imaged spectra enables an *in situ* determination of any crystal artefacts and the variance of the multiple nominally identical spectra determines the spectral radiance random uncertainty. The potassium acid phthalate crystals were cylindrically bent to a radius of either 15.24 cm or 22.86 cm and are located 410 cm from the source. The data are recorded on Kodak RAR 2492 film. The instrument spectral resolution is limited by the crystal and was measured³² in the wavelength $\lambda \approx 7\text{--}10 \text{ \AA}$ range to be $\lambda/\delta\lambda \approx 800\text{--}1,000$. Each spectrometer covers a range of approximately 5–6 \AA . The data were recorded over 6–16 \AA , but here we report only data from 7–12.7 \AA . At shorter wavelengths the data require additional corrections for backlight variability and at longer wavelengths the data require corrections for second-order crystal reflections and possibly sample self-emission. Work to perform these corrections is in progress.

Transmission and opacity analysis. The spectrometers record 20–24 spectrally resolved and spatially resolved images from each experiment, from different viewing angles and with different spectral ranges. The 22 experiments discussed here required analysis of more than 450 spectral images. We regard this data set as the minimum needed to provide benchmark-quality opacity tests, because such tests require^{15,16}

- (1) multiple measurements to determine simultaneously the attenuated and unattenuated signals, to provide random uncertainty evaluations, and to reject artificial features from crystal defects;
- (2) transmission measurements with different areal densities, in order to extend the dynamic range and verify proper scaling with sample thickness according to the Beer–Lambert–Bouguer Law;
- (3) repeated experiments to verify reproducibility;
- (4) tamper-only experiments to verify the transmission accuracy;
- (5) measurements with different T_e/n_e conditions to help unravel multiple entangled processes; and
- (6) experiments with different tamper materials to evaluate possible systematic errors.

Each spectrally resolved image is digitized and corrected for the spatial magnification and spectral dispersion. The film optical density is converted to exposure³³ and agreement among measurements obtained at varying exposures with different diagnostic configurations and sample thicknesses confirmed the conversion accuracy. Multiple methods were developed to obtain the transmission. Here, we summarize the method for the five experiments conducted with a CH + Be tamper (Extended Data Fig. 2 and Extended Data Table 1). Four spectrometers recorded data at $\pm 9^\circ$ on each experiment, two with crystals of radius 15.24 cm (designated CCP4a and CCP10a) and two with crystals of radius 22.86 cm (designated CCP4b and CCP10b). Three of these experiments employed a FeMg ‘half-moon’ design and two used a tamper-only sample. The 9° spectrometer angle of view combined with the measured $\sim 1.5 \text{ mm}$ backlight-to-sample distance³⁴ implies that the $+9^\circ$ spectrometer views the backlight centre through the FeMg portion of the ‘half-moon’ sample and the -9° spectrometer views the backlight centre through the tamper-only

portion. Thus, the spectrally resolved transmission can be inferred by dividing the $+9^\circ$ spectrometer signal by the -9° spectrometer signal.

The measurements using the crystals of radii 15.24 cm and 22.86 cm are analysed as two separate groups to avoid possible crystal reflectivity differences. The unattenuated measurements demonstrate the reproducibility for these five experiments (Extended Data Fig. 2a). The absolute fractional percentage standard deviation $[\sigma/I]_{\text{abs}}$ averaged over 8–12 \AA was $\pm 5.8\%$ and the relative fractional percentage standard deviation $[\sigma/I]_{\text{rel}}$ was $\pm 3.3\%$. Therefore, we use the mean spectral intensity to represent the unattenuated spectrum.

The attenuated and unattenuated spectral intensities used to determine the transmission on experiment Z2624 are shown in Extended Data Fig. 2b. The transmissions from each crystal on Z2624 are shown in Extended Data Fig. 2c. The error bars represent 1σ uncertainties obtained by convolving the uncertainties in the attenuated and unattenuated measurements. The dashed lines correspond to the fractional transmission uncertainty. The transmission uncertainty averaged over the 8.5–12.5 \AA range that provides the best accuracy is $\pm 10\%$ for both the CCP10a and CCP10b spectrometers. These are independent measurements of the same physical quantity and the uncertainty in the mean absolute transmission is therefore approximately $\pm 7\%$. The relative uncertainty as a function of wavelength is of the order of $\pm 2\%$, but the exact value depends on the wavelength range considered.

The optical depth obtained by taking the natural log of the mean transmission measured on Z2624 (Extended Data Fig. 2d) includes Fe and Mg contributions. To proceed, we calculate the Mg optical depth with the PrismSPECT model³⁵ using the Mg areal densities determined with RBS. The iron optical depth is inferred by subtracting the Mg calculation from the FeMg result. The mean opacity from the three Be-tamped iron opacity experiments is shown in Extended Data Fig. 2e, along with the fractional uncertainties. These results are then combined (Extended Data Fig. 2f) to infer an overall mean opacity for the Be-tamped experiment conditions. The opacity uncertainty is $\pm 10\%$ over a broad wavelength range, rising to $\pm 15\%$ near the short-wavelength end of the spectrum. This relatively small uncertainty is obtained by averaging repeated experiments that each provide multiple opacity measurements.

Systematic error evaluation. The estimated $\pm 10\%$ opacity uncertainty over the 8.5–12.5 \AA range is small compared to the 30–400% differences between the Be-tamped measurement and the opacity models (Fig. 3). Discrepancies of this order, their persistence for all tested opacity models, and their importance for both astrophysics and laboratory experiments make it essential to consider possible systematic errors. An additional concern is that the data exceed the cold opacity³⁶ by $\sim 36\%$ (Extended Data Fig. 3a) averaged over the 7–8 \AA range. Revisiting the opacity of room-temperature iron may be warranted because the stated uncertainty of generally accepted³⁷ cold iron opacity measurements is $\pm 10\%$, but recent measurements³⁸ are approximately 40% higher. Nevertheless, it is only possible for the hot iron plasma opacity to exceed the cold opacity in a particular wavelength range if there is an important contribution from either bound–bound or resonant bound–free transitions. According to the SCRAM model, the bound–bound contribution falls to 50% at $\sim 9.5 \text{ \AA}$ and it shrinks for shorter wavelengths (Extended Data Fig. 3b). Furthermore, the combination of bound–bound and bound–free features is expected to obey the oscillator strength sum rule³⁹. This states that the total oscillator strength for a given initial state to all final states is equal to the number of electrons. Accordingly, if models underpredict the opacity in a certain wavelength range, then there should be a compensating overprediction in another wavelength range. Work is in progress to measure opacity values for the strong $n = 2$ to $n = 3$ (n is the principal quantum number) iron L-shell transition arrays that fall in the 12.5–16 \AA range. This could provide insight into the most suitable interpretation of the sum rule.

The systematic error evaluation comprised the majority of the work conducted for this project and here we provide only a synopsis of the results. The systematic errors are divided into three categories according to the direction in which they bias the result with respect to the true value: those that always reduce inferred opacity, those that always increase the inferred opacity, and those that can do either, depending on the conditions. The systematic error evaluation incorporates both experimental tests and experimentally benchmarked simulations. The simulations were performed using the HELIOS⁴⁰ one-dimensional radiation-hydrodynamics code using measured radiation source characteristics and the experimental geometry. The simulation credibility was supported by the calculated sample temperature and density, which match the experimentally measured values for a wide variety of experiments that included changes in the tamper and sample thicknesses and compositions.

Initial systematic error tests evaluated whether the transmission scaled with the areal density according to the Beer–Lambert–Bouguer Law¹⁶. This scaling was obeyed within the experiment uncertainties (Extended Data Fig. 4), which mitigates concerns^{15,16} from transmission determination errors, extraneous background, tamper self-emission, and spatial non-uniformities. Satisfying this relationship is necessary, but not always sufficient, to detect possible systematic errors. Therefore, alternative experimental and simulation-based tests were conducted.

Sample contamination and tamper shadowing are possible systematic errors that can cause an overestimate of the inferred opacity. The RBS sample characterization verified that the oxygen contamination was 10–100 times lower than the amount needed to cause a 10% change in the opacity. Other contaminants were smaller and their contamination did not notably bias the result. We reiterate that the incident heating radiation, backlight radiation, diagnostic set-up, and data analysis methods are the same for all the experiments. The tamper is the only experimental set-up change between the lower- T_e/n_e results that agree reasonably well with opacity calculations¹⁷ to the present higher- T_e/n_e results that strongly disagree. Therefore, we investigated whether increasing the tamper thickness biases the experimental result.

Tamper shadowing can occur when the tamper used to infer the unattenuated spectrum is hotter than the tamper behind the FeMg layer, because the FeMg absorbs some fraction of the incident photons. If the attenuation in the shadowed tamper is larger, then the inferred iron opacity would be larger than the true value. The quantitative influence of tamper shadowing on the opacity depends on the T_e and n_e values. The shadowing effect on the opacity grows monotonically with increasing wavelength, is smaller for thinner FeMg layers, and smaller for thinner or less-attenuating tampers. Simulations⁴⁰ estimate negligible effects for all the CH tampers at wavelengths less than approximately 10.5 Å. However, at longer wavelengths, tamper shadowing is calculated to cause a significant (>5%) change in the inferred opacity for the 70- μm -thick CH tamper. This concern motivated our replacement of part of the thick CH tamper with Be. The Be attenuation is less than for an equivalent mass of CH and is negligible for the range of possible T_e/n_e conditions. A comparison of the Be-tamped results with the thick-CH-tamped results confirmed that there was little difference in the inferred opacity below 10.5 Å. The thick-CH-tamped results presented here were corrected for the shadowing effect in the 10.5–12.7 Å range using the simulation results. However, this introduces a possible error that is difficult to quantify. Therefore, we regard the Be-tamped results to be the most accurate.

Possible systematic errors that cause an underestimate of the inferred opacity include extraneous background, tamper self-emission, and iron self-emission. The first two effects are similar: they both add an extra signal that is not altered by the iron absorption to both the attenuated and unattenuated spectra, causing the inferred iron opacity to be lower than the true value. The imaging spectrometers account for the spatially homogeneous background, but spatially imaged extraneous background could arise, for example, from plasma that emerges from the Z-pinch dynamic hohlraum near the end of the experiment. Tamper self-emission is also expected to be small. However, both the emerging Z-pinch plasma and the tamper might emit over a long time in comparison to the backlight duration. The 1-mm-wide Ti aperture installed between the sample and the spectrometer lines of sight restricts the observed plasma volume and helps mitigate these effects.

Nevertheless, there is one finding that could suggest that either extraneous background or tamper self-emission is present: for some experiments the observed Mg He α and He β transmissions are approximately 15% higher at the line centre than models predict. This might suggest that the true opacity near these wavelengths is higher than reported here, increasing the discrepancy with iron opacity model predictions. This observation could also be affected by the large optical depths of these lines at the line centre; for these lines the radiation transport calculations are complex. Furthermore, Beer–Lambert–Bouguer scaling tests with varying thickness of iron provide evidence that extraneous background and tamper self-emission are not important. In addition, the general agreement between iron opacities inferred with CH and CH + Be tampers indicates that tamper self-emission is unimportant. Finally, HELIOS simulations also predict small contributions from the CH self-emission. These multiple investigations provide evidence that extraneous background and tamper self-emission are unimportant, but a definitive conclusion awaits an explanation for the higher-than-expected Mg He α and He β transmission values.

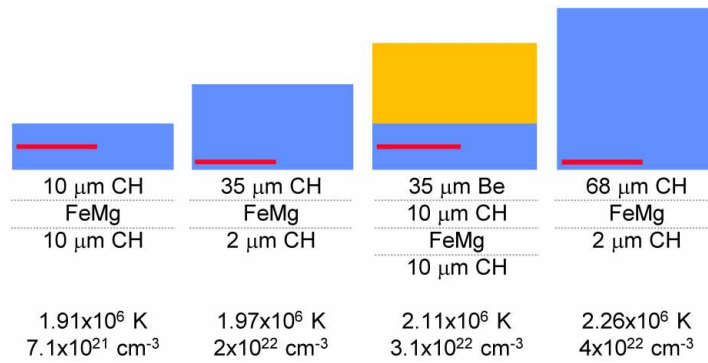
The effect of iron self-emission tends to be largest for optically thick lines and for the long wavelength portion of the spectrum. Calculations using HELIOS⁴⁰ simulations that account for the fact that the iron self-emission might persist longer than the backlight duration show that iron self-emission causes less than a 20% effect on the inferred opacity in the 7–12.7 Å region. Both Beer–Lambert–Bouguer scaling tests and the lack of any observed iron emission lines from the portion of the

sample that is heated, but not backlit, provide experimental evidence that the iron self-emission is small. We therefore do not correct the inferred opacity reported here for self-emission.

Effects that could either raise or lower the inferred opacity include sample areal density errors, transmission errors, spatial non-uniformities, temporal non-uniformities, deviations from LTE, and plasma diagnostic errors. Sample areal density errors are precluded by the RBS and interferometry measurements described above. Systematic transmission errors were investigated by analysing tamper-only experiments—where the transmission is known to equal unity—with the same methods applied to the FeMg ‘half-moon’ samples. The transmission deviations were found to be comparable to or less than the estimated uncertainty. Spatial non-uniformities were directly measured using specially designed samples⁴¹ and were estimated using HELIOS simulations⁴⁰. The effects were found to be small. Temporal non-uniformity effects estimated using HELIOS simulations were small. Deviations from LTE were investigated using the PrismSPECT model³⁵ to calculate the FeMg plasma transmission in both LTE and non-LTE at the plasma T_e and n_e values inferred from the LTE Mg K-shell spectral analysis. The non-LTE calculations included the radiation field at the sample using measurements of the time-dependent radiation source spatial distribution and the geometric dilution. The main effects predicted by these calculations are a slight decrease in the average ionization and a ground-state population increase. The latter increases the strong spectral feature opacities, decreases the valleys between these strong features and therefore notably increases the discrepancy between model predictions and measurements of iron opacity. Finally, the displayed model–experiment comparisons employed the nominal T_e/n_e values obtained from an LTE analysis of the Mg K-shell spectra²². Iron opacity calculations were also done using the SCRAM model over the range of the T_e/n_e uncertainties (Extended Data Fig. 5). The calculations at the lowest T_e value and the highest n_e value agree slightly better with the measurements, but the improvement is small compared to the model–experiment discrepancy.

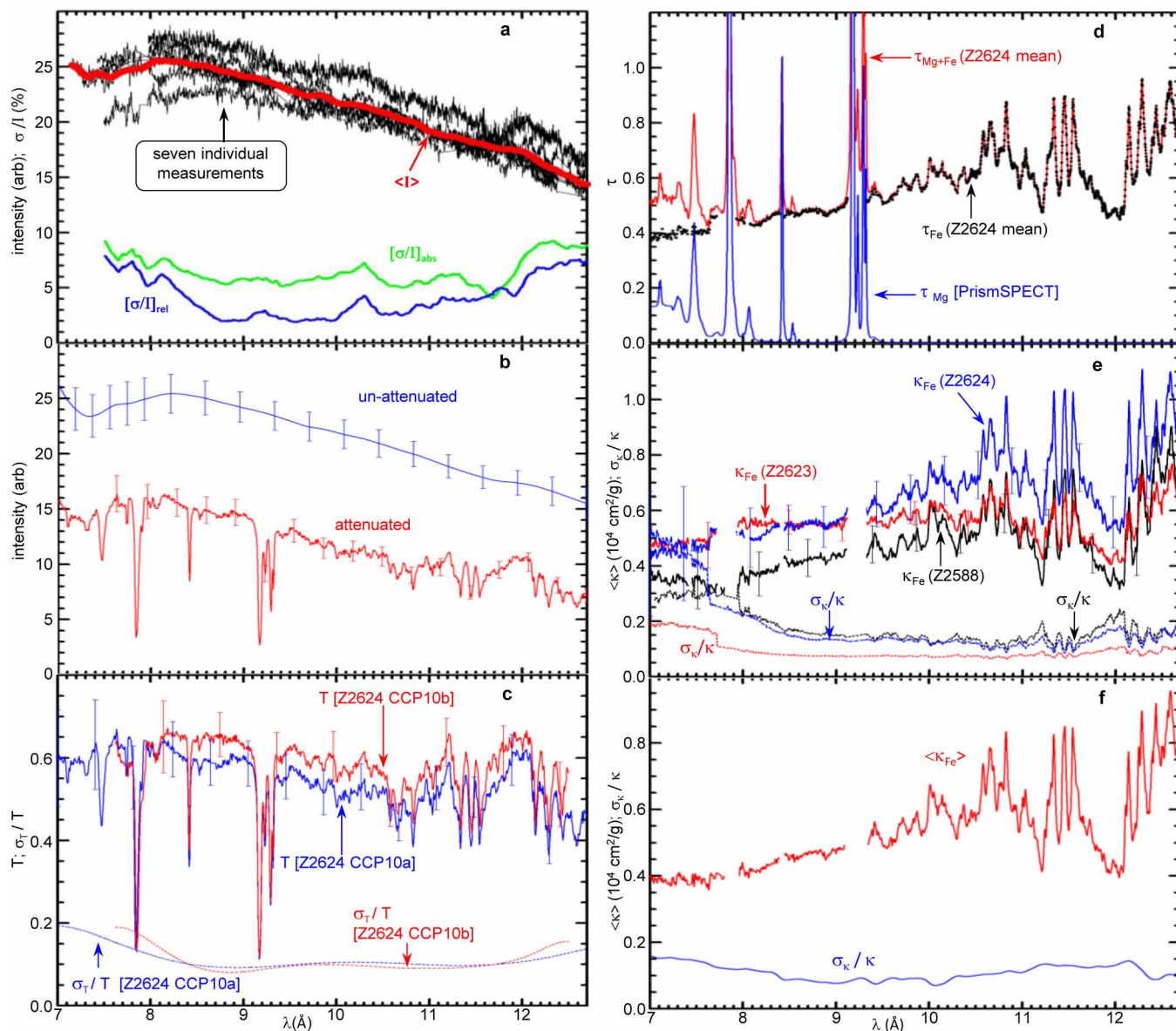
Eleven different potential systematic errors were evaluated. None appears to explain the reported discrepancy between opacity model calculations and the iron opacity data. If the data are correct, then our understanding of radiation interactions with atoms in high-energy-density plasma must be revised. Given the impact on both astrophysics and laboratory physics, continued scrutiny of the existing data and execution of new experiments designed to test hypotheses for the model–experiment discrepancies is warranted.

29. Bailey, J. E. *et al.* Dynamic hohlraum radiation hydrodynamics. *Phys. Plasmas* **13**, 056301 (2006).
30. Bailey, J. E. *et al.* Diagnosis of x-ray heated Mg/Fe opacity research plasmas. *Rev. Sci. Instrum.* **79**, 113104 (2008).
31. Jaynes, C., Barradas, N. P. & Szilágyi, E. Accurate determination of quantity of material in thin films by Rutherford backscattering spectrometry. *Anal. Chem.* **84**, 6061–6069 (2012).
32. Loisel, G. *et al.* A methodology for calibrating wavelength dependent spectral resolution for crystal spectrometers. *Rev. Sci. Instrum.* **83**, 10E133 (2012).
33. Henke, B. L. *et al.* Low-energy x-ray response of photographic films. II. Experimental characterization. *J. Opt. Soc. Am. B* **1**, 828–849 (1984).
34. Nagayama, T. *et al.* Parallax diagnostics of radiation source geometric dilution for iron opacity experiments. *Rev. Sci. Instrum.* **85**, 11D603 (2014).
35. MacFarlane, J. J. *et al.* in *Proc. Int. Symp. on Inertial Fusion Science and Applications (Monterey, California, 2003)* 457–464 (American Nuclear Society, 2003).
36. Henke, B. L., Gullikson, G. M. & Davis, J. C. X-ray interactions: photoabsorption, scattering, transmission, and reflection at E=50–30,000 eV, Z=1–92. *At. Data Nucl. Data Tables* **54**, 181–342 (1993).
37. del Grande, N. K. L. Shell photoabsorption spectroscopy for solid metals: Ti, V, Cr, Fe, Ni, Cu. *Phys. Scr.* **41**, 110–114 (1990).
38. Zheng, L., Cui, M.-Q., Zhu, J. & Zhao, Y.-D. Determination of the photoabsorption cross-sections of Al and Fe films in the soft x-ray region using synchrotron radiation. *High Energy Phys. Nuclear Phys.* **28**, 1121–1125 (2004).
39. Cowan, R. D. *The Theory of Atomic Structure and Spectra* (Univ. California Press, 1981).
40. MacFarlane, J. J., Golovkin, I. E. & Woodruff, P. R. HELIOS-CR—a 1-D radiation-magnetohydrodynamics code with inline atomic kinetics modeling. *J. Quant. Spectrosc. Radiat. Transf.* **99**, 381–397 (2006).
41. Nagayama, T. *et al.* Investigation of iron opacity experiment plasma gradients with synthetic data analyses. *Rev. Sci. Instrum.* **83**, 10E128 (2012).



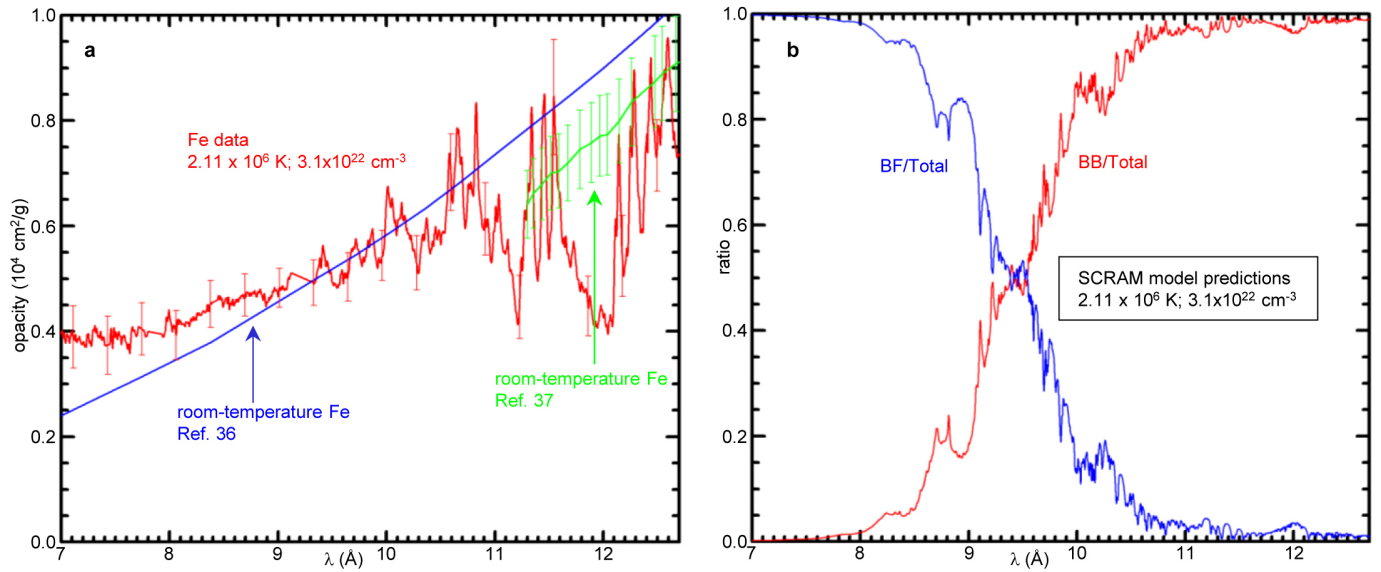
Extended Data Figure 1 | Schematic diagram of four sample configurations used in Z opacity experiments. The FeMg layer (red line) is completely encapsulated by the CH (blue) in order to avoid exposure to atmosphere during the experiment preparation. One sample type employed a Be tamper (yellow) to provide additional tamping while greatly reducing both the attenuation and

emission in comparison with CH. T_e and n_e both increase as the tamper mass increases. The tamper thicknesses and the resulting average T_e and n_e values²² are listed below each sample type. Experiments were also conducted using the same tamper construction, but without the FeMg layer, to provide calibrations of the opacity measurement accuracy.



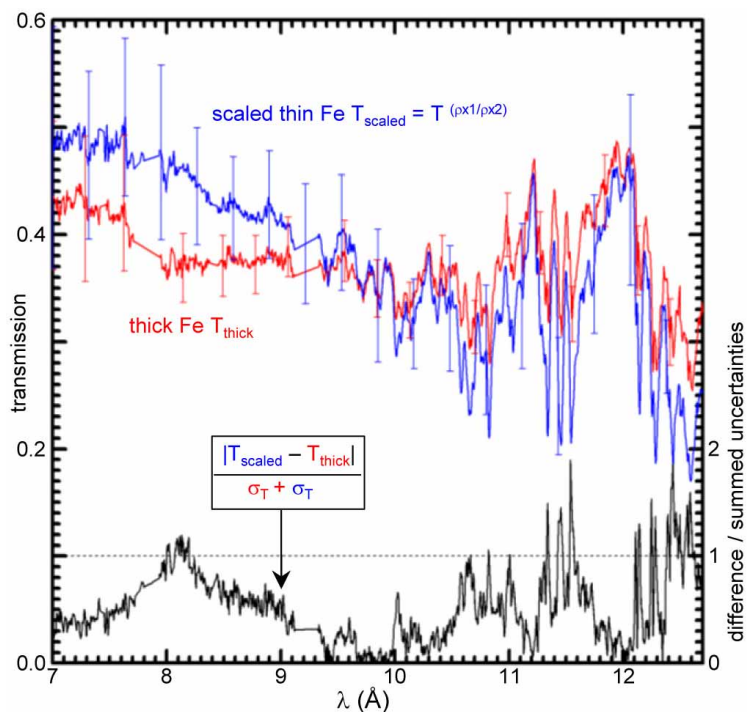
Extended Data Figure 2 | Data illustrating the transmission determination method. The five experiments shown here were conducted with a CH + Be tamper. **a**, The seven measurements of the unattenuated spectral intensity I from five experiments using the CCP4a and CCP10a spectrometers are denoted with black lines. The mean spectral intensity $\langle I \rangle$ (red) is used to determine transmission, $[\sigma/I]_{\text{abs}}$ represents the absolute percentage unattenuated spectrum 1σ uncertainty (green), and $[\sigma/I]_{\text{rel}}$ represents the relative percentage unattenuated spectrum 1σ uncertainty as a function of wavelength (blue). A similar collection of data are obtained from the seven CCP4b and CCP10b spectrometer measurements. (arb, arbitrary units). **b**, The attenuated (red) and unattenuated (blue) spectral intensities used to determine the transmission on experiment Z2624. These data were recorded with the CCP4a and CCP10a crystals and a

similar data set (not shown) was recorded with the CCP4b and CCP10b crystals. **c**, The transmissions T measured on Z2624 agree within the 1σ uncertainties. **d**, The optical depth (τ , red) inferred by taking the natural log of the mean transmission measured on Z2624 includes contributions from both Fe and Mg. The optical depth corresponding to the iron contribution only (black) is inferred by subtracting the Mg contribution calculated with PrismSPECT³⁵ (blue) from the FeMg mixture measurement. **e**, The mean opacities κ inferred from the three Be-tamped iron opacity measurements (solid), along with 1σ fractional absolute uncertainties (dashed). **f**, These measurements are combined to infer the overall mean opacity ($\langle \kappa \rangle$, red) and associated 1σ fractional uncertainty (blue) for these conditions. The error bars in **b**, **c**, and **e** represent the 1σ uncertainty.



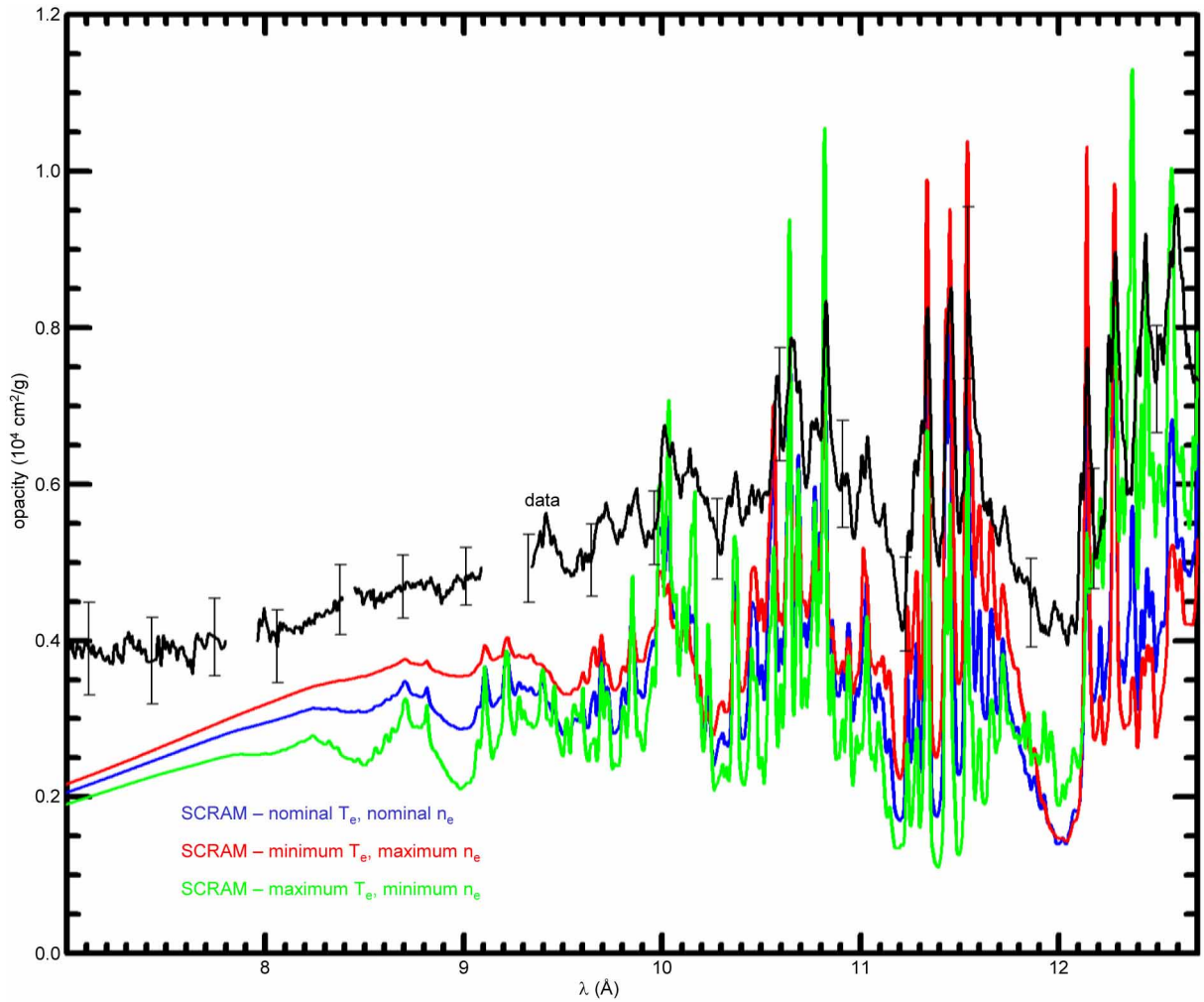
Extended Data Figure 3 | The measured Z iron opacity exceeds the room-temperature value³⁶ for wavelengths where models predict the opacity is dominated by photoionization. **a**, The measured iron opacity from the Be-tamped result is larger than the room-temperature value^{36,37} for wavelengths shorter than approximately 9 \AA . The error bars correspond to 1σ uncertainties.

b, The SCRAM opacity model predicts that the ratio of the bound-free (BF) opacity contribution with the total opacity (blue) is larger than the ratio of the bound-bound (BB) opacity contribution with the total (red) for wavelengths less than approximately 9.5 \AA .



Extended Data Figure 4 | Beer-Lambert-Bouguer scaling test for Be-tamped iron opacity data. The transmission should scale according to $T_2 = T_1^{N_{x2}/N_{x1}}$, where N_{x1} and N_{x2} are areal densities associated with transmissions T_1 and T_2 . The thick iron sample transmission T_{thick} ($NX \approx 1.91 \times 10^{18}$ atoms per cm^2) is shown in red (left axis). The average transmission for the two experiments using a thin iron sample

($NX \approx 0.98 \times 10^{18}$ atoms per cm^2) was scaled by the ratio of the areal densities (T_{scaled} ; blue). The error bars represent 1σ uncertainties. A quantitative evaluation is provided by taking the ratio of the transmission difference with the summed 1σ uncertainties (black; right axis). Values below unity (dashed black) satisfy the scaling test.



Extended Data Figure 5 | Evaluation of changes in the model–data comparisons at the error bounds determined for the plasma conditions. The measured iron opacity at $T_e = 2.11 \times 10^6 \text{ K}$ and $n_e = 3.1 \times 10^{22} \text{ cm}^{-3}$ is denoted with a black line, with error bars corresponding to the 1σ uncertainty.

SCRAM²³ calculations are shown at the nominal conditions in blue, at the minimum T_e , maximum n_e in red and at the maximum T_e , minimum n_e in green. The minimum T_e , maximum n_e values lead to the lowest ionization and the maximum T_e , minimum n_e values lead to the highest ionization.

Extended Data Table 1 | Sample specifications for Z opacity experiments

Shot	Date	Top Be (μm)	Top CH (μm)	Bottom CH (μm)	Total CH (μm)	Fe ($\times 10^{18} \text{ cm}^{-2}$)	Mg ($\times 10^{18} \text{ cm}^{-2}$)	construction
2176	March 2011	----	67	2	69	2.065 ± 0.095	1.02 ± 0.022	5 layers Mg/Fe; Fe; 5 layers Al/Fe
2219	June 2011	----	----	----	20	----	----	CH only
2221	June 2011	----	10	10	20	0.640 ± 0.034	0.746 ± 0.045	10 layers Fe/Mg
2242	August 2011	----	67	2	69	1.307 ± 0.04	1.260 ± 0.03	10 layers Fe/Mg
2243	August 2011	----	----	----	70	----	----	CH only
2244	August 2011	----	67	2	69	2.967 ± 0.08	1.187 ± 0.005	10 layers Fe/Mg
2267	Dec. 2011	----	67	2	69	2.837 ± 0.045	1.32 ± 0.065	20 layers Fe/Mg
2268	Dec. 2011	----	69	2	71	----	----	CH only; $\sim 250\text{\AA}$ NaF in middle
2270	Dec. 2011	----	68	2	70	1.277 ± 0.095	1.330 ± 0.091	20 layers Fe/Mg
2299	Feb. 2012	----	10	10	20	----	----	CH only; $\sim 250\text{\AA}$ NaF in middle
2301	Feb. 2012	----	10	10	20	0.382 ± 0.017	0.828 ± 0.038	Co-sputtered FeMg
2309	March 2012	----	10	10	20	----	----	CH only; $\sim 250\text{\AA}$ NaF in middle
2363	June 2012	----	35	2	37	1.295 ± 0.005	1.29 ± 0.01	Co-sputtered FeMg
2364	June 2012	----	70	2	72	0.659 ± 0.002	1.24 ± 0.0	Co-sputtered FeMg
2365	June 2012	----	67	2	69	----	----	CH only; $\sim 250\text{\AA}$ NaF in middle
2366	June 2012	----	70	2	72	0.659 ± 0.002	1.24 ± 0.0	Co-sputtered FeMg
2389	July 2012	----	10	10	20	----	----	CH only; $\sim 250\text{\AA}$ NaF in middle
2588	Dec. 2013	35	10	10	20	1.04	1.25	Co-sputtered FeMg
2589	Dec. 2013	35	10	10	20	----	----	Be+CH Tamper; $\sim 250\text{\AA}$ NaF in middle of CH
2623	March 2014	35	10	10	20	1.91	1.17	Co-sputtered FeMg
2624	March 2014	35	10	10	20	0.926	1.40	Co-sputtered FeMg
2625	March 2014	35	10	10	20	----	----	Be+CH Tamper; $\sim 250\text{\AA}$ NaF in middle of CH

The areal density uncertainties correspond to the standard deviation of multiple RBS measurements. A dash denotes that the component was not present.